Thermal Expansion and Defect Chemistry of MgO-Doped $Sm_2Zr_2O_7$

Zhixue Qu, Chunlei Wan, and Wei Pan*

State Key Laboratory of New Ceramics and Fine Processing, Department of Materials Science and Engineering, Tsinghua University, Beijing 100084, China

Received June 18, 2007. Revised Manuscript Received July 18, 2007

A series of solid solutions of $(Sm_{2-x}Mg_x)Zr_2O_{7-x/2}$ pyrochlores were prepared by a solid-state reaction and characterized by X-ray diffraction, high-temperature dilatometry, Raman spectroscopy, and X-ray photoelectron spectroscopy. X-ray diffraction and Raman spectroscopy reveal that MgO doping does not break down the pyrochlore structure of $Sm_2Zr_2O_7$ for all of the samples, though it increases the degree of structure disorder. However, the thermal expansion coefficient is remarkably increased through doping up to $x = 0.075$ with a maximum value around 11.94×10^{-6} K^{-1} (room temperature to 1000 °C), which can mitigate the mismatches of thermal expansion in the high-temperature applications of $Sm_2Zr_2O_7$. A new solid−solution mechanism that is different from previous research was proposed and confirmed by analyzing the variation of the lattice parameters, experimental density, and X-ray photoelectron spectroscopy of samples. It involves the transformation of the solid−solution model about Mg^{2+} interstitial and substitution with a turning point at composition point $x = 0.075$. This transformation and consequently the variation of lattice energy may be responsible for the variation of the thermal expansion coefficient.

Introduction

In the past few decades, rare-earth zirconate pyrochlores have been of keen concern because of their special structure and good high-temperature phase stability. The oxide pyrochlore structure, of ideal stoichiometry $A_2B_2O_6O'$, crystallizes in the space group $Fd\bar{3}m$ and may be considered as an ordered defective fluorite structure (Figure 1, with origin at the B site). Compared with the ideal fluorite structure, there is a crystallographical unoccupied anion site with a specific atom position in the pyrochlore structure. The intrinsic existence of anion vacancy ensures that pyrochlore compounds exhibit some interesting properties, for instance, the fast oxygen ion conductivity and low thermal conductivity. A variety of actual and potential applications have been reported, such as, solid electrolytes,[1,2] catalysts,[3,4] nuclear waste disposal,[5−7] and thermal barrier coatings (TBCs).[8−11]

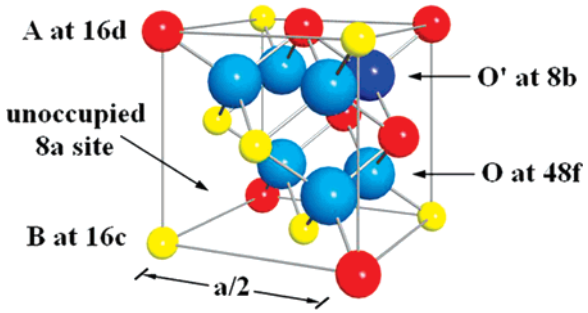

Figure 1. Partial unit cell of the pyrochlore structure. The red sphere represents the A cation at the 16d site; the yellow one, the B cation at the 16c site; the light-blue one, the oxygen anion at the 48f site; and the dark-blue sphere stands for the oxygen anion at the 8b site.

Nearly all of these applications involve high-temperature processes, and thus it is integral to investigate the thermal expansion behavior of these materials at high temperature, which can affect the thermal expansion compatibility with other components in the device. Kutty et al.[12] have measured the linear thermal expansion coefficients (TEC) of a series of rare-earth zirconate pyrochlores $Ln_2Zr_2O_7$ (Ln = La, Nd, Sm, Eu, Gd), which fall in the range of $8-11 \times 10^{-6}$ K^{-1} within the temperature range 298−1500 K, and came to a conclusion that the TEC value increases with decreasing ionic radius, that is, it increases from $La_2Zr_2O_7$ to $Gd_2Zr_2O_7$. Schelling et al.[13] have summarized the TEC values of $La_2Zr_2O_7$, $Sm_2Zr_2O_7$, and $Gd_2Zr_2O_7$ to be 9.1×10^{-6}, 10.8×10^{-6}, and 11.6×10^{-6} K^{-1} (293−1273 K), respectively. Unfortunately, for most of the application cases, the TEC

* To whom correspondence should be addressed. E-mail: panw@tsinghua.edu.cn. Tel: +86-10-62772858. Fax: +86-10-62771160.

(1) Kutty, K. V. G.; Mathews, C. K.; Rao, T. N.; Varadaraju, U. V. *Solid State Ionics* **1995**, *80*, 99−110.
(2) Shimura, T.; Komori, M.; Iwahara, H. *Solid State Ionics* **1996**, 86−8, 685−689.
(3) Sohn, J. M.; Woo, S. I. *Catal. Lett.* **2002**, *79*, 45−48.
(4) Sohn, J. M.; Kim, M. R.; Woo, S. I. *Catal. Today* **2003**, *83*, 289−297.
(5) Sickafus, K. E.; Minervini, L.; Grimes, R. W.; Valdez, J. A.; Ishimaru, M.; Li, F.; McClellan, K. J.; Hartmann, T. *Science* **2000**, *289*, 748−751.
(6) Ewing, R. C.; Weber, W. J.; Lian, J. *J. Appl. Phys.* **2004**, *95*, 5949−5971.
(7) Lutique, S.; Staicu, D.; Konings, R. J. M.; Rondinella, V. V.; Somers, J.; Wiss, T. *J. Nucl. Mater.* **2003**, *319*, 59−64.
(8) Vassen, R.; Cao, X. Q.; Tietz, F.; Basu, D.; Stover, D. *J. Am. Ceram. Soc.* **2000**, *83*, 2023−2028.
(9) Padture, N. P.; Gell, M.; Jordan, E. H. *Science* **2002**, *296*, 280−284.
(10) Wu, J.; Wei, X. Z.; Padture, N. P.; Klemens, P. G.; Gell, M.; Garcia, E.; Miranzo, P.; Osendi, M. I. *J. Am. Ceram. Soc.* **2002**, *85*, 3031−3035.
(11) Wan, C. L.; Pan, W.; Xu, Q.; Qin, Y. X.; Wang, J. D.; Qu, Z. X.; Fang, M. H. *Phys. Rev. B* **2006**, *74*, 144109.
(12) Kutty, K. V. G.; Rajagopalan, S.; Mathews, C. K.; Varadaraju, U. V. *Mater. Res. Bull.* **1994**, *29*, 759−766.
(13) Schelling, P. K.; Phillpot, S. R.; Grimes, R. W. *Philos. Mag. Lett.* **2004**, *84*, 127−137.

10.1021/cm071615z CCC: $37.00
Published on Web 09/11/2007

values of rare-earth zirconate pyrochlores are much lower than those of other components in the device ($\sim 17.5 \times 10^{-6}$ K^{-1} for bond-coat NiCoCrAlY in the TBC system of the gas turbine, for example), and the thermal expansion mismatch may then lead to stress, which is chiefly responsible for the failure of the whole device.

As is known, the change in crystal cell volume due to lattice vibrations is closely related to the variation of lattice energy, which can be achieved by altering the concentration of the defects in the crystal. The doping method is expected to introduce various kinds of defects and change the lattice energy of the crystal, resulting in the variation of the TECs. Several studies on the theoretical calculation of divalent oxides doping into rare-earth zirconates[14,15] have been reported. Calculations for the solution energy related to divalent element doping were carried out by Wilde and Catlow[14] and by Pirzada et al.[15] All of the calculations showed that substitution would take place at the trivalent A cation site, and the concentration of the oxygen anion vacancy would increase with doping of divalent oxides, which may simultaneously increase the oxygen ion conductivity and reduce the thermal conductivity. However, there has been no experimental report to confirm the calculations and to investigate the influence of divalent oxide doping on the thermal expansion behavior of materials.

In present work, we investigated the variation of thermal expansion behavior of $Sm_2Zr_2O_7$ pyrochlore with doping of the divalent oxide MgO and discussed the solution mechanism of divalent ion Mg^{2+} doping into the lattice of $Sm_2Zr_2O_7$ pyrochlores. A significant enhancement of TEC by doping was observed, and a quite different solid−solution model from previous calculations was proposed.

Experimental Section

Materials. All of the samples were prepared in a conventional solid-state reaction. Samaria (Rare-Chem Hi-Tech Co., Ltd., purity ≥99.99%), magnesia (Beijing-Chem Co., A.R., purity ≥98.0%), and zirconia (Farmeiya Advanced Materials Co., Ltd., purity ≥99.9%, including 2.57% HfO_2) powders were used as starting materials. The mixtures with stoichiometry $(Sm_{2-x}Mg_x)Zr_2O_{7-x/2}$ ($x = 0$, 0.025, 0.050, 0.075, 0.100, 0.150, 0.200, 0.300) were ball-milled with ethanol for 24 h and dried using a rotary evaporator. Then, the specimens were pressed and sintered at 1600 °C for 10 h in an air atmosphere, during which the solid-state reaction and densification proceed simultaneously. Bulk densities of the sintered samples measured according to the Archimedes principle showed that the samples were almost fully densified in the in situ solid-state reaction.

Characterization. Phase identification and analysis were conducted by X-ray diffraction (XRD). Two kinds of XRD scans were performed using an X-ray diffractometer (Rigaku, D/max-RB, Japan) with nickel-filtered Cu Kα radiation. Continuous scans (6 °/min) were used for qualitative phase identification, while slow step scans at a rate of 0.01 °/2 s were conducted to determine the shifts of the X-ray spectrum and hence the lattice parameters. Lattice parameters of the solid solutions were calculated from slow step scan XRD data, using the least-squares method. The Raman spectra of samples were recorded at room temperature on a microscopic confocal Raman spectrometer (Renishaw, RM2000, U.K.) using an argon ion laser with radiation at 514.5 nm. The laser beam was focused on a freshly polished surface under a microscope, and the width of the analyzed spot was ~2 μm. The full power of the incident beam was 4.7 mW. The accuracy for the wavenumber values of the Raman spectra is 1 cm^{-1}. To ascertain the homogeneity of the samples, several spots were detected for each sample. The signal was collected at a rate of 600 cm^{-1}/30 s and accumulated for a three-times scan. X-ray photoelectron spectroscopy (XPS) investigations were performed using a PHI Quantera SXM XPS spectrometer with Al Kα radiation ($h\upsilon = 1486.6$ eV) as the excitation source. The samples were polished and cleaned to make a new surface visible, and Ar^+ sputtering was used to remove surface contaminations. A carbon layer with a binding energy of 284.8 eV (C 1s) was deposited onto the surface to calibrate the binding energy shifts due to surface charging effects. The XPS analysis was conducted at ambient temperature in an analysis chamber with a pressure of 6.7×10^{-8} Pa. The linear thermal expansion coefficients of the specimens were obtained from measurements of the temperature-dependent change of length using a high-temperature dilatometer (Model NETZSCH DIL 402EP, Germany). The dimensions of the sintered rod specimens after machining were approximately $4.5 \times 4 \times 40$ mm^3. The data were recorded continuously at a scanning rate of 5 °C/min, within the range from the ambient temperature to 1375 °C in air.

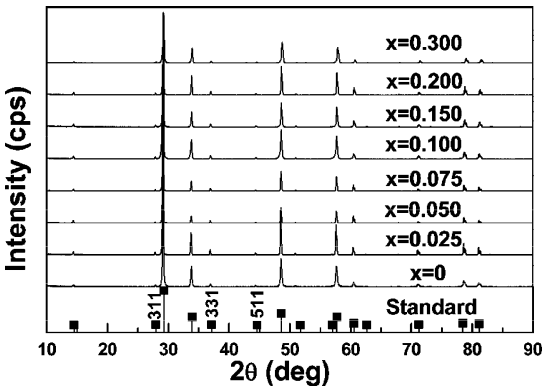

Figure 2. XRD patterns of all of the compositions and standard (24−1012).

Results and Discussion

Phase Identification and Thermal Expansion Behavior. X-ray diffraction (XRD) patterns from a continuous scan, as shown in Figure 2, reveal that all of the patterns of the samples are well consistent with the standard XRD spectrum of $Sm_2Zr_2O_7$ (ICDD PDF No. 24−1012), though there is slight shifts of the peaks, and no appreciable peak of MgO or other compounds can be observed, which indicates that the solid solutions of $(Sm_{2-x}Mg_x)Zr_2O_{7-x/2}$ are formed, and the upper limit of solid−solution region may be greater than $x = 0.300$.

The synthesized single-phase solid solutions were characterized by high-temperature dilatometry. Figure 3 shows the temperature dependence of the thermal expansion rate $\Delta L/L_0$ for the samples. All of the data of the samples keep in good linearity when the temperature is above 300 °C, which suggests the temperature insensitivity of the TEC at high temperature. It can also be seen from Figure 3 and its

(14) Wilde, P. J.; Catlow, C. R. A. *Solid State Ionics* **1998**, *112*, 173−183.
(15) Pirzada, M.; Grimes, R. W.; Maguire, J. F. *Solid State Ionics* **2003**, *161*, 81−91.

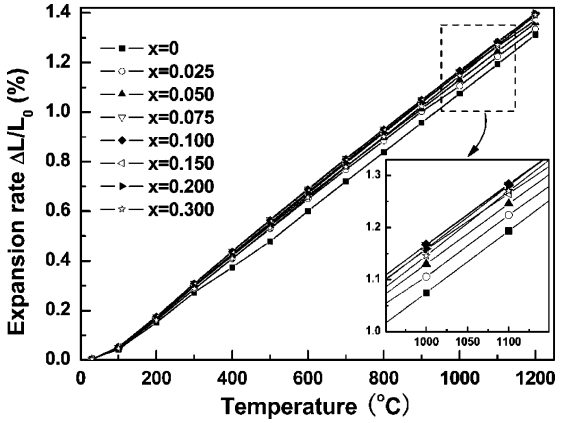

Figure 3. Thermal expansion rate as a function of temperature for $(Sm_{2-x}Mg_x)Zr_2O_{7-x/2}$ samples. Partial enlarged detail from 950 °C to 1150 °C (inset).

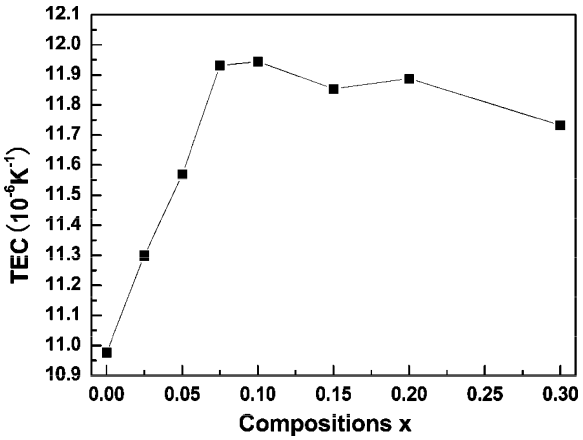

Figure 4. Composition dependence of the average thermal expansion coefficient for $(Sm_{2-x}Mg_x)Zr_2O_{7-x/2}$ samples within the temperature range from room temperature to 1000 °C. The line is a guide to the eye.

inset that the expansion rates of the doping samples are all greater than that of the pure $Sm_2Zr_2O_7$, and there is an increase with increasing doping content when composition x is smaller than 0.075.

The trend can be seen more clearly from Figure 4, which shows the composition dependence of the average thermal expansion coefficients for $Sm_2Zr_2O_7$ with various contents of MgO, within the temperature range from room temperature to 1000 °C. In Figure 4, we can see that the thermal expansion coefficients increase rapidly with increasing doping content of MgO up to $x = 0.075$, followed by a decrease at a slight slope, and the composition $x = 0.075$ turns up to be a turning point. The TECs of the samples with compositions of $x \geq 0.075$ are all above 11.7×10^{-6} K^{-1} with a maximum value of 11.94×10^{-6} K^{-1} at $x = 0.100$. For pure $Sm_2Zr_2O_7$, the corresponding value is 10.97×10^{-6} in this study, which is close to 10.8×10^{-6} K^{-1} in the literature.[13] Comparing the TEC values of pure and doped $Sm_2Zr_2O_7$, we can see that a remarkable enhancement has been achieved through the doping of MgO, which can mitigate the mismatches of TECs with other components, especially with metallic ones.

Structure Analysis. From the XRD patterns of the samples in Figure 2, the occurrence of super-lattice 311, 331, and 511 peaks,[10] which are marked in the figure, suggests the presence of a pyrochlore phase for all of the samples. It

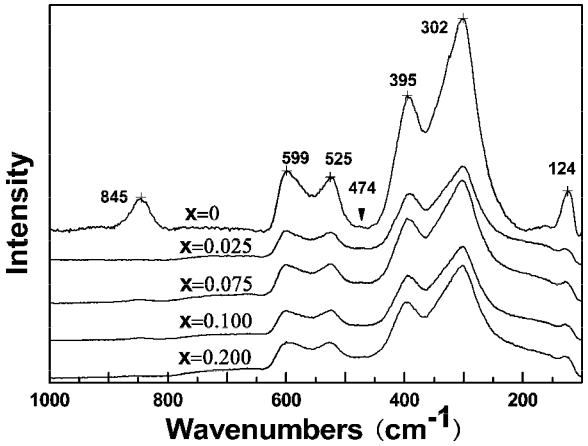

Figure 5. Raman spectra of representative compositions: $x = 0$, 0.025, 0.075, 0.100, and 0.200.

Table 1. Factor Group Analysis for the Pyrochlore Structure[a]

	Distribution of degrees of freedom			Number of normal modes		
O_h	A and B cations, D_{3d} 16(d), 16(c)	O anion C_2 48(f)	O′ anion T_d 8(b)	acoustic modes	lattice modes	selection rules
A_{1g}	0	1	0	0	1	Raman
A_{2g}	0	0	0	0	0	inactive
E_g	0	1	0	0	1	Raman
T_{1g}	0	2	0	0	2	inactive
T_{2g}	0	3	1	0	4	Raman
A_{1u}	0	0	0	0	0	inactive
A_{2u}	2	1	0	0	3	inactive
E_u	2	1	0	0	3	inactive
T_{1u}	4	3	1	1	7	infrared
T_{2u}	2	2	0	0	4	inactive

[a] Refs 16 and 21.

can also be confirmed by Raman spectra, which were shown in Figure 5. Factor group analysis[16−21] (Table 1) of $A_2B_2O_7$ pyrochlores has predicted the appearance of six Raman-active modes (R) and seven infrared-active modes (IR) for the vibration spectra, which can be represented as follows.

$$\Gamma = A_{1g}(R) + E_g(R) + 4T_{2g}(R) + 7T_{1u}(IR) \qquad (1)$$

All of these six Raman-active modes of pyrochlore structure can be observed in Figure 5 for all of the samples. According to the polarized Raman measurements in the literature,[17,19,20] the Raman bond at 525 cm^{-1}, which can display significant intensity changes with different polarization directions, is assigned to the A_{1g} mode. The most intense Raman-active bond at 302 cm^{-1} is identified as the E_g mode, whereas the other three vibrational frequencies at 395, 599, 845 cm^{-1} may be assigned to three of the four T_{2g} modes. There is a much weaker peak at 474 cm^{-1} (arrow in the figure), which may be considered to be the fourth T_{2g} mode.[16]

(16) Scheetz, B. E.; White, W. B. *J. Am. Ceram. Soc.* **1979**, *62*, 468−470.
(17) Vandenborre, M. T.; Husson, E.; Chatry, J. P.; Michel, D. *J. Raman Spectrosc.* **1983**, *14*, 63−71.
(18) Gupta, H. C.; Brown, S.; Rani, N.; Gohel, V. B. *J. Raman Spectrosc.* **2001**, *32*, 41−44.
(19) Hess, N. J.; Begg, B. D.; Conradson, S. D.; McCready, D. E.; Gassman, P. L.; Weber, W. J. *J. Phys. Chem. B* **2002**, *106*, 4663−4677.
(20) Zhang, F. X.; Manoun, B.; Saxena, S. K.; Zha, C. S. *Appl. Phys. Lett.* **2005**, *86*, 181906.
(21) Michel, D.; Perez y Jorba, M.; Collongues, R. *Mater. Res. Bull.* **1974**, *9*, 1457−1468.

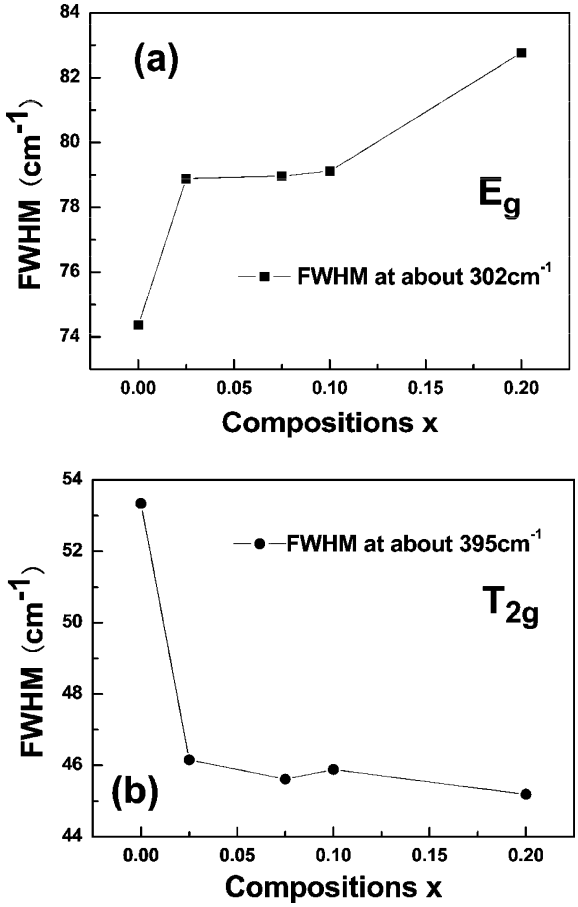

Figure 6. Composition dependence of the full widths at half-maximum (fwhm) of Raman-active modes. (a) the E_g mode at 302 cm^{-1}, (b) the T_{2g} mode at 395 cm^{-1}.

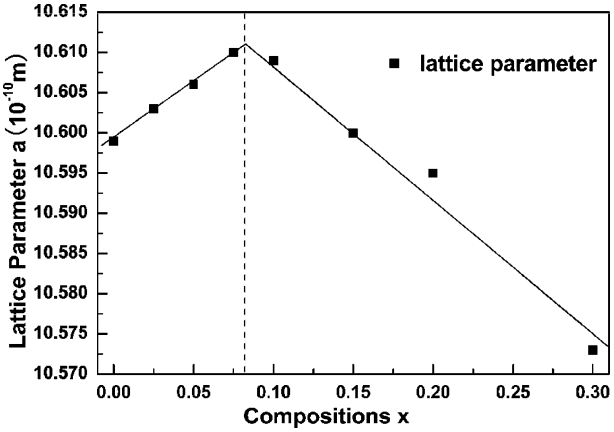

Figure 7. Lattice parameters as a function of MgO doping content at room-temperature. The solid lines in the left and right parts of figure are fit lines using the least-squares method for the compositions of *x* below and above 0.075, respectively.

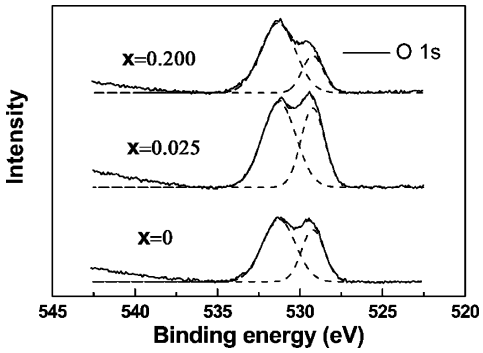

Figure 8. Oxygen 1s XPS spectra and the corresponding Gaussian functional fitted curves of representative compositions. $x = 0$, 0.025, and 0.200.

As for the frequencies below 200 cm^{-1} (only 124 cm^{-1} in this study), similar cases were observed by Vandenborre et al.[17] in the titanate spectra, and the lines were not considered to be fundamental frequencies, which was attributed to anharmonic effects or disorder in the materials.

Comparing the Raman spectra of representative compositions with each other, we can see that all of the band intensities decrease with the doping of MgO, which may suggest that the degree of disorder of the crystals increases with the doping. Moreover, the full widths at half-maximum (fwhm) of the Raman-active mode were investigated, as shown in Figure 6. It can be seen from part (a) of Figure 6 that the fwhm of the E_g mode at 302 cm^{-1} increases with the increasing doping content *x*, as did those of the vibrational frequencies at 525 and 599 cm^{-1}, which are not shown here. The T_{2g} mode at 395 cm^{-1} is the only line whose fwhm decreases with increasing doping content *x* (part (b) of Figure 6). Factor group analysis shows that of all six of the Raman-active modes, there is only one T_{2g} mode related to the 8b site oxygen anion, whereas all of the other modes are related to the 48f site oxygen anion. Consequently, the T_{2g} mode at 395 cm^{-1} is considered as the one related to the 8b site oxygen anion.

It is believed that the Raman line broadening is due to structural disorder or lattice strain.[16,19] So, the increase of the fwhm of the E_g mode, which is related to the vibrations of the 48f oxygen anion, implies an increasing degree of the 48f oxygen anion disorder, whereas the decrease of that of the T_{2g} mode at 395 cm^{-1} may suggest that there is little change at the 8b site other than it becoming ordered because of the similar decrease in intensity. The anion disorder between the 48f and 8a sites may be responsible for the former disorder. Moreover, a turning point appears in the increasing line of part (a) of Figure 6 at around $x = 0.075-0.100$ instead of a linear increase, which may suggest a change of the solid−solution model around the range of compositions $x = 0.075-0.100$.

Defect Chemistry and Solution Model. To investigate the solid−solution mechanism, the defects formation model in the crystal was discussed according to the variation of lattice parameters, experimental densities, and XPS spectra. The calculated lattice parameters as a function of the doping content of MgO are shown in Figure 7. Composition point $x = 0.075$ appears as a turning point again, and the lattice parameters initially increase linearly when $x \leq 0.075$, followed by a decrease with a larger slope. In the case of experimental bulk density, it can be seen from Figure 10 that it has similar trends with lattice parameters. The initial simultaneous increase of lattice parameters and experimental density implies that the total atomic mass of a unit cell is increasing with the doping of MgO first, which suggests the presence of an interstitial atom, whereas the presence of a turning point near $x = 0.075$, which coincides with the case of the fwhm of the E_g mode in Raman spectra, may suggest a change in the solid−solution model. A solution process

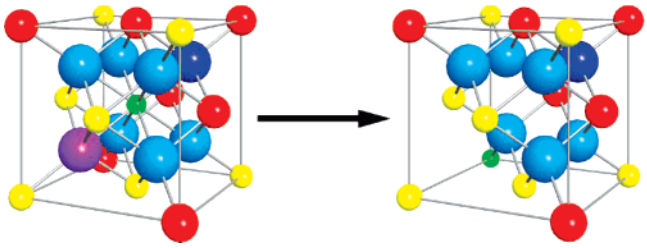

Figure 9. Imagined figures of magnesium interstitial and substitution model for illustration. Magnesium ion (green), samarium ion (red), zirconium ion (yellow), oxygen anion at the 48f site (light-blue), oxygen anion at the 8b site (dark-blue), and oxygen interstitial atom at the 8a site (purple).

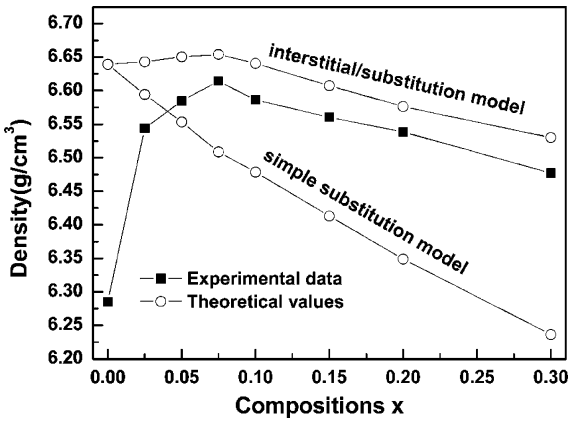

Figure 10. Experimental and theoretical densities of $(Sm_{2-x}Mg_x)Zr_2O_{7-x/2}$ samples. The sample of $Sm_2Zr_2O_7$ without MgO is not very dense. The line is a guide to the eye.

Table 2. Shannon Effective Ionic Radii for Selected Ions in Å[a]

ions	charge	coordination	ionic radii
Mg	2	VI	0.72
		VIII	0.89
Zr	4	VI	0.72
Sm	3	VIII	1.079

[a] Ref 22.

involving substitution may be implied by the following decrease.

The Shannon effective ionic radii[22] of the several cations referred to in this work are shown in Table 2. Because of the smaller ionic radius of Mg^{2+}, an interstitial process is the exclusive way to increase the lattice parameters. For the following substitution process, if a Mg^{2+} ion substitutes for a Zr^{4+} ion that is 6-fold coordination in the pyrochlore structure, the ionic radii of two ions are almost the same (~0.72 Å). It is impossible for this case to decrease the lattice parameters rapidly. However, when the substitution process occurs at the Sm^{3+} site, which is 8-fold coordination, the ionic radius of the Mg^{2+} ion is much smaller than that of the Sm^{3+} ion, which may result in the rapid decrease in the lattice parameters after the turning point.

X-ray photoelectron spectroscopy, which is sensitive to the evolution of the chemical environment of an element in the disordered materials, was conducted to confirm the substitution process of Mg^{2+} ions. As shown in Figure 8, all of the oxygen 1s spectra split into two peaks and can be fitted by two Gaussian functions. Similar cases have also been observed by Chen et al.[23,24] when they investigated another pyrochlore compound $Gd_2Ti_2O_7$, and the variations of the oxygen 1s spectra were analyzed to confirm the anion disordering in the materials.

As we know, the binding energy of oxygen is related to the electronegativity of the neighboring atoms. The greater the electronegativity of the surrounding atoms is, the lower the average electron density on the element will be, and lower effective negative charge density leads to higher binding energy. For the neighboring cations in this work, it is known from literature[25] that the Pauling electronegativities of magnesium, zirconium, and samarium ions are 1.31, 1.33, and 1.17, respectively.

From the structure image of pyrochlore shown in Figure 1, we can seen that there are two different oxygen sites: a 48f site that is coordinated by two samarium and two zirconium ions and an 8b site that is surrounded by four samarium ions. Because of the higher electronegativity of the zirconium ion than that of the samarium ion, the peak with a higher binding energy is assigned to oxygen ions at the 48f site, whereas the one with lower binding energy is related to oxygen ions at the 8b site.

It can also be seen in Figure 8 that the intensities of the two split peaks for the compositions before the turning point $x = 0.075$ are very close, and there is no appreciable variation between the spectra. However, when the composition is beyond the turning point ($x = 0.200$), the peak with higher binding energy reduces rapidly. From the data mentioned above, we know that the electronegativities of magnesium and zirconium ion are similar and each is greater than that of the samarium ion. At the initial section of doping range, no substitution occurs around oxygen ions, leading to little variation of oxygen 1s XPS spectra. For the following section, if a Mg^{2+} ion substitutes for a Zr^{4+} ion, there will still be no dramatic change for the spectra, as a result of the similar electronegativities of the magnesium and zirconium ions, which is not consistent with the rapid reduction observed. However, if the Sm^{3+} ion is substituted for the Mg^{2+} ion, the higher electronegativity of the Mg^{2+} ion will increase the chemical environment similarity of some 8b sites with 48f sites leading to the decrease of the peak that is corresponding to oxygen ions at the 8b site. Moreover, the substitution of a Sm^{3+} ion for a Mg^{2+} ion can also result in line broadening of the peak that is corresponding to oxygen ions at the 48f site, which can be observed in Figure 8. Thus, the substitution of a Sm^{3+} ion for a Mg^{2+} ion at the composition range of $x \geq 0.075$ is confirmed.

Hence, the solid−solution mechanism for MgO doping, we believe, involves both interstitial and substitution processes. When the doping content is less than 0.075, magnesium and oxygen interstitial ions should be the defect pair in the solid solution. The oxygen ion may take the site of the 8a vacancy, whereas the magnesium ion occupies the interstice in the simple cubic oxygen array (left figure in Figure 9). The interstitial ions expand the lattice, and result

(22) Shannon, R. D. *Acta Crystallogr.* **1976**, *A32*, 751−767.
(23) Chen, J.; Lian, J.; Wang, L. M.; Ewing, R. C.; Boatner, L. A. *Appl. Phys. Lett.* **2001**, *79*, 1989−1991.
(24) Chen, J.; Lian, J.; Wang, L. M.; Ewing, R. C.; Wang, R. G.; Pan, W. *Phys. Rev. Lett.* **2002**, *88*, 105901.
(25) Rohrer, G. S. *Structure Bonding in Crystalline Materials*; Cambridge University Press: New York, 2001.

in an increase in the lattice parameters and the cell volume. However, the mass of the unit cell increases simultaneously due to the interstitial ions, which is more remarkable to increase the bulk density. When the concentration of interstitial atoms is above a certain value ($x = 0.075$), the interaction of defect pairs may increase the energy, and then substitution will take place at the site of the Sm^{3+} ion (right figure in Figure 9). Because of the smaller ionic radius of the Mg^{2+} ion than that of the Sm^{3+} ion (Table 2), the substitution leads to the following decrease in the lattice parameters and the cell volume, but a faster decrease in the mass of the unit cell induced by the large atomic mass difference results in a decrease in density.

On the basis of the above analysis, several solid−solution models were proposed, and the theoretical densities of the samples were calculated from the corresponding molecular weight and the lattice parameters. Comparing the theoretical densities of proposed models with the experimental values, the model in best agreement can be represented in Kröger−Vink notation as follows.

When the composition is $x \leq 0.075$,

$$MgO + V_O^{\cdot\cdot} \rightarrow Mg_i^{\cdot\cdot} + O_O \quad (2)$$

And it is followed by eq 3 when the composition is $x \geq 0.075$,

$$3MgO \xrightarrow{Sm_2O_3} Mg_i^{\cdot\cdot} + 2Mg'_{Sm} + 3O_O \quad (3)$$

The theoretical densities of this interstitial/substitution model are shown in Figure 10 by the upper curve. The other theoretical curve were calculated according to the simple substitution model reported by Wilde and Catlow[14] and by Pirzada et al.[15] The solid−solution process of this model can be simply represented by eq 4.

$$2MgO \xrightarrow{Sm_2O_3} 2Mg'_{Sm} + V_O^{\cdot\cdot} + 2O_O \quad (4)$$

It can be seen from Figure 10 that the line corresponding to this simple substitution model is monotonically decreasing and is below the line of the experimental data when the composition is about $x \geq 0.05$, which indicates that the model fails to explain the solution reaction. Pirzada et al.[15] have reported that the formation energy of the divalent dopant interstitial in pyrochlore $A_2B_2O_7$ is 1.3−6.9 eV, which was the main reason why they did not consider the divalent dopant interstitial ion compensation. However, the defect formation energy of the 8a oxygen interstitial is below −10 eV, which has been calculated by Wilde and Catlow.[14] So, the occupation of the oxygen vacancy at the 8a site provides the possibility of the occurrence of a magnesium interstitial. Moreover, the more than 30% smaller ionic radius of the Mg^{2+} ion than that of the Sm^{3+} ion may also be responsible for the failure of the simple substitution model.

Generally speaking, the thermal expansion of materials is directly related to their crystal structure and atom bonding. In the $A_2B_2O_7$ pyrochlore structure, of all of the atom positions, 48f oxygen sites within the A_2B_2 tetrahedra are off-center and a positional parameter, ϵ, which describes the position of the 48f oxygen, should be determined. Parameter ϵ, which usually lies between 0.3125 and 0.375, determines the A−O/B−O distance and the exact shapes of BO_6 and AO_8 polyhedra.[26,27] Previous work[12,28] has shown that the bonding strength is correlated to the variation of parameter ϵ, and the Madelung energy decreases with increasing ϵ value. In light of the interstitial/substitution model above, up to $x = 0.075$, oxygen ions take the position of the unoccupied 8a site (left figure in Figure 9), which increases the ϵ value because of the repulsion, and thus the Madelung energy decreases with the increasing composition *x*, resulting in an increase in thermal expansion coefficients. When the composition is $x \geq 0.075$, a fraction of Mg^{2+} ions is substituted for the Sm^{2+} ions and no more 8a oxygen interstitial atoms increase (right figure in Figure 9). The lower valence of the Mg^{2+} ion relaxes the bond with the O^{2-} ion, and ZrO_6 makes a more perfect octahedron, which decreases the ϵ value and consequently increases the Madelung energy. Hence, the thermal expansion coefficients vary inversely with the Madelung energy which decreases initially and then increases.

Conclusions

In this work, a series of solid solutions of $(Sm_{2-x}Mg_x)$-$Zr_2O_{7-x/2}$ with a pyrochlore structure were prepared by a solid-state reaction. The effects of MgO doping on thermal expansion coefficients and crystal structure have been investigated, and the doping mechanism has been discussed in detail. High-temperature dilatometric results demonstrate that there is a remarkable enhancement of the linear thermal expansion coefficients due to the MgO doping at the composition range of $x \leq 0.075$ followed by a slight slope decrease as $x > 0.075$. The turning point at $x = 0.075$ was also observed in the composition dependence curves of the fwhm of Raman spectra, the lattice parameters, and experimental density, which indicates the change of the solid−solution model. From the analysis of the variation of lattice parameters, experimental density, and X-ray photoelectron spectroscopy of the samples, we propose a new solid−solution model, which is quite different from previous research, that is, when the doping content is $x \leq 0.075$, magnesium interstitial is the dominant defect in the solid solutions; when the doping content is above $x = 0.075$, magnesium substitution will take place at the site of the Sm^{3+} ion. This transformation of the defect model and consequently the variation of the lattice energy may be responsible for the variation of the thermal expansion coefficient. This work provides the possibility of tailoring the thermal expansion properties through changing the crystal structure of the materials by doping. In addition, the enhancement of TECs can mitigate the mismatches of thermal expansion in the high-temperature applications of $Sm_2Zr_2O_7$.

Acknowledgment. This work was supported by the National Natural Science Foundation of China (Grants 50232020 and 50572042).

CM071615Z

(26) McCauley, R. A. *J. Appl. Phys.* **1980**, *51* (1), 290−294.
(27) Chakoumakos, B. C. *J. Solid State Chem.* **1984**, *53*, 120−129.
(28) Pannetier, J. *J. Phys. Chem. Solids* **1973**, *34*, 583−589.